Nonreciprocal surface plasmons in angularly varying magnetized cylindrically rolled graphene

Yarden Mazor*
School Of Electrical Engineering, Tel Aviv University, Tel Aviv 69978, Israel

(Received 20 February 2024; revised 1 July 2024; accepted 8 July 2024; published 6 August 2024)

We analytically and numerically study the nonreciprocal surface waves guided by a magnetized graphene tube. When applying the magnetic bias perpendicularly to the cylinder axis, the conductivity profile cross section is nonuniform due to the varying angle between the magnetic bias and the surface-wave guiding tube, which enables us to obtain pronounced nonreciprocal modes with different field distributions for propagation in opposite directions due to the coupling between different values of orbital angular momentum. We show that this property can be leveraged for directional power delivery when changing the source location, and we study the isolation ratio as a function of different parameters. The dependence of the isolation ratio on the magnetic field bias allows simple, yet robust, control over the nonreciprocal wave propagation properties.

DOI: 10.1103/PhysRevB.110.085410

I. INTRODUCTION

Cylindrical structures are among the most common waveguide geometries being used. Prominent examples include coaxial waveguides and hollow metallic tubes [1]. The dispersion of guided waves can be controlled by varying the cylinder size (potentially also the internal cylinder in a coaxial geometry) and the distribution and properties of the filling material. These waveguides have many uses, such as communications [1], open-ended aperture antennas [2,3], material sensing probes, and more.

More recently, incorporating metamaterials and metasurfaces within a cylindrical geometry was examined as a platform for various applications. Scattering from cylindrical metasurface structures was studied in [4] to achieve cloaking, and in [5], the authors showed how to systematically analyze and synthesize a layered cylindrical structure to achieve different scattering functionalities. Another venue is tailoring guided wave properties in cylindrical waveguides using metasurfaces coating the waveguide walls or serving as the waveguide themselves. This is a particularly interesting avenue since cylindrical guided modes exhibit complex polarization states, helicity, and spin–orbital angular momentum (OAM) coupling [6]. This was pioneered in [7], where a helically slotted perfect electric conducting (PEC) cylinder was studied. A modal theory for such structures with general electric impedance walls was formulated in [8]. In [9], a metamaterial lining was used to control the cutoff and modal properties, and Ref. [10] showed how general bianisotropic walls can be used to tailor the modal dispersion, field distribution, and spin. A step forward was taken in [11], where the authors discussed an actual implementation and considered realistic constraints and the arising dispersion effects. Such structures also appear in more natural systems, where the most prominent example is carbon nanotubes. The electrodynamics of cylindrical graphene-based structures was first studied in [12], where the appropriate boundary conditions were formulated and the dispersion of guided surface waves was carefully mapped. In the last decade, several groups have fabricated and measured artificial cylindrical graphene structures for enhancing light-matter interaction [13,14], four-wave mixing [15], and all-optical modulation [16]. Multilayered folding is shown in [17], and additional applications are reviewed in [18].

An equally important ingredient of this work is the nonreciprocal propagation of waves. Nonreciprocal waveguides have many applications, such as routing and sorting of signals and serving as building blocks in the design of nonreciprocal components such as isolators and circulators [19,20]. To obtain significant nonreciprocal behavior, such as different field distributions for oppositely propagating fields which can be leveraged for isolation [1] (e.g., asymmetrically ferrite loaded waveguides) or one-way guiding, one has to incorporate nonreciprocity with some form of structural asymmetry [21,22]. In the context of tubelike structures, [23] studied guided waves in several cylindrical geometries incorporating graphene, where electrical bias (controlling the chemical potential μ_c) and magnetic bias were used as control parameters to manipulate the wave characteristics. Importantly, this work also incorporated nonreciprocity since the magnetic field bias gives rise to an asymmetric conductivity tensor of the graphene layer. Nevertheless, this nonreciprocity did not visibly manifest in the modal dispersion or field distribution due to the highly "symmetric" magnetic bias scheme considered—a radial magnetic field bias.

In this work, we examine the nonreciprocal wave propagation on a magnetized cylindrical impedance surface, such as graphene. Unlike in other examples, where the structural asymmetry requires inhomogeneous cross-section materials or scatterer parameters, here, it stems from the magnetic biasing scheme itself. By applying a simple magnetic bias perpendicular to the axis of the guiding cylindrical surface (represented by a thin impedance sheet, see Fig. 1), an

*Contact author: Yardenm2@tauex.tau.ac.il

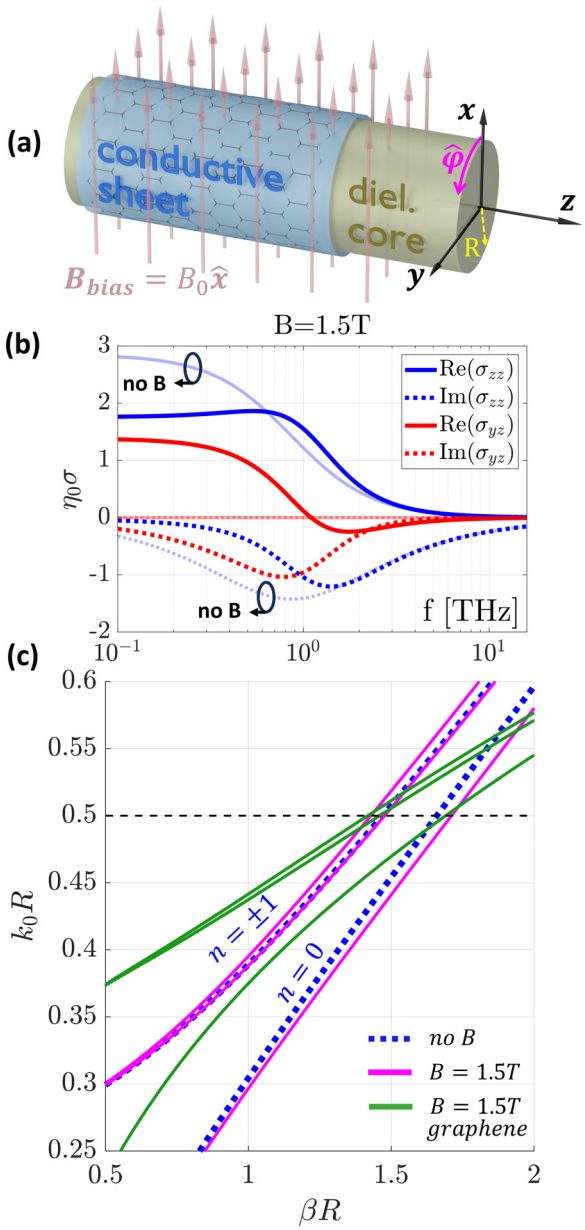

FIG. 1. (a) Geometry of a magnetically biased graphene tube. (b) Graphene conductivity σ under an external magnetic bias of $B_0 = 1.5$ T in the $\hat{x}$ direction. Transparent lines show the conductivity with no magnetic bias. ($\eta_0\sigma$ is plotted, where $\eta_0 = \sqrt{\mu_0/\epsilon_0}$ is the vacuum impedance and $e^{j\omega t}$ is the time conversion is used). (c) Surface wave dispersion. Blue shows the case with no external magnetic bias (showing $n = 0$ and $n = \pm 1$ dispersion branches); magenta shows the case with external magnetic bias (many n's now contribute to each dispersion branch due to structural inhomogeneity caused by the magnetic bias). Both assume conductivity constant at $f = 4$ THz in Eqs. (15) and (16); hence, the vertical axis corresponds to varying R. Green shows the case with external magnetic bias accounting for the frequency dispersion of graphene conductivity according to Eqs. (15) and (16), with $R = 6$ μm. Graphene parameters are given below Eq. (17).

azimuthally dependent conductivity tensor arises. Therefore, the external magnetic bias itself provides both the nonreciprocity and the spatial inhomogeneity. This, in turn, creates coupling between different values of OAM of the guided wave components. The nonreciprocity makes this coupling asymmetric, giving rise to complex nonreciprocal waves composed of a superposition of different cylindrical eigenfunctions (each with its characteristic OAM), resulting in different field distribution modes propagating in opposite directions. This will be shown to enable directional excitation using simple dipolar sources as a function of the source location and spin-momentum coupling.

II. FORMULATION

A. Uniform conductivity

Let us start from the basic formulation of the problem of waveguiding by thin cylindrical shells. Although the examples we provide are based on a graphene system, this formulation can be applied to waveguiding by any thin, cylindrical, conductive sheet (such as cylindrical metasurfaces). Throughout this paper we use an $e^{j\omega t}$ time dependence. Since the waves propagate essentially in free space (with the addition of the impedance/surface susceptibility boundary condition), we can represent them as a superposition of the "standard" TE and TM modes:

$$E_z = \begin{Bmatrix} A_n^i I_n(\alpha r), & r < R \\ A_n^o K_n(\alpha r), & r > R \end{Bmatrix} e^{-j\beta z} e^{-jn\varphi}, \tag{1a}$$

$$H_z = \begin{Bmatrix} B_n^i I_n(\alpha r), & r < R \\ B_n^o K_n(\alpha r), & r > R \end{Bmatrix} e^{-j\beta z} e^{-jn\varphi}, \tag{1b}$$

with $\beta^2 = \alpha^2 + k_0^2$, $k_0 = \omega\sqrt{\mu\epsilon}$, and I_n and K_n being the modified Bessel functions of the first and second kind. The other field components can be directly derived from Eqs. (1a) and (1b) and are given in Appendix A for completeness.

In the present problem, the waves are guided by a tube of radius R, which satisfies the surface impedance boundary condition

$$\hat{\boldsymbol{r}} \times (\boldsymbol{H}_{\text{out}} - \boldsymbol{H}_{\text{in}})_{r=R} = \boldsymbol{J}_s = \underline{\underline{\sigma}} \boldsymbol{E}_{\tan, r=R}, \tag{2}$$

where $\underline{\underline{\sigma}}$ is the 2×2 surface conductivity matrix, which can be written explicitly as

$$\underline{\underline{\sigma}} = \begin{bmatrix} \sigma_{\varphi\varphi} & \sigma_{\varphi z} \\ \sigma_{z\varphi} & \sigma_{zz} \end{bmatrix}, \tag{3}$$

and $\boldsymbol{E}_{\tan}$ is the electric field components tangent to the tube. In addition to this, since the cylindrical surface hosts only electric surface currents, the tangential electric fields need to be continuous,

$$E_z(R^+) = E_z(R^-), \; E_\varphi(R^+) = E_\varphi(R^-), \tag{4}$$

where $(\cdot)^+$ and $(\cdot)^-$ indicate sampling of the fields on the surface of the tube on the outer and inner sides, respectively. Using this condition, the field representation on the surface of the tube can be reduced to rely on two coefficients $A_n^i, \bar{B}_n^i = \eta_0 B_n^i$, with $\eta_0 = \sqrt{\mu_0/\epsilon_0} \approx 377\Omega$ being the intrinsic impedance of vacuum (see Appendix A). If we now define

$$\boldsymbol{D}_n = \begin{pmatrix} A_n^i \\ \bar{B}_n^i \end{pmatrix}, \tag{5}$$

we can represent the operations required for substitution into Eq. (2) as

$$\boldsymbol{E}^{o}_{n,\tan}(r=R) = \boldsymbol{E}^{i}_{n,\tan}(r=R) = \underline{\underline{\boldsymbol{M}}}_{E,n}\boldsymbol{D}_n, \quad (6a)$$

$$\hat{\boldsymbol{r}} \times (\boldsymbol{H}^{o}_{n} - \boldsymbol{H}^{i}_{n})_{(r=R)} = \underline{\underline{\boldsymbol{M}}}_{H,n}\boldsymbol{D}_n, \quad (6b)$$

with

$$\underline{\underline{\boldsymbol{M}}}_{E,n} = \begin{bmatrix} \frac{n\bar{\beta}}{\bar{\alpha}^2} I_n & -\frac{j\bar{k}_0}{\bar{\alpha}} I'_n \\ I_n & 0 \end{bmatrix}, \quad \underline{\underline{\boldsymbol{M}}}_{H,n} = \begin{bmatrix} 0 & -\frac{1}{\bar{\alpha}K'_n} \\ -\frac{j\bar{k}_0}{\bar{\alpha}K_n} & \frac{n\bar{\beta}}{\bar{\alpha}^3 K'_n} \end{bmatrix}. \quad (7)$$

To shorten the notation, we will omit the argument of the modified Bessel functions I_n and K_n and their derivatives I'_n and K'_n when we refer to sampling them on the surface of the tube. In addition, we have defined $\bar{\alpha} = \alpha R$, $\bar{\beta} = \beta R$, and $\bar{k}_0 = k_0 R$. Now, if we substitute this representation into the boundary condition given in Eq. (2) and assume the conductivity $\underline{\underline{\boldsymbol{\sigma}}}$ is independent of φ, we obtain the eigenmode equation

$$\left(\eta_0 \underline{\underline{\boldsymbol{\sigma}}}\,\underline{\underline{\boldsymbol{M}}}_{E,n} - \underline{\underline{\boldsymbol{M}}}_{H,n}\right)\boldsymbol{D}_n = 0. \quad (8)$$

For this equation to have a nontrivial solution for the coefficient vector $\boldsymbol{D}_n$, the determinant of the bracketed matrix must vanish, which yields the dispersion relation as a determinant of a 2×2 matrix. For any value of n (the OAM of the mode) and angular frequency ω we substitute, we will obtain $\beta(\omega)$, the dispersion relation of the nth mode. Substituting this value back will yield the modal coefficients A^i_n and $\bar{B}^i_n$, forming a mixed TE/TM mode, with the amplitude of each constituent depending on the conductivity.

B. Angularly varying conductivity

Based on the previous section, our goal now is to describe the waves propagating in a system where $\underline{\underline{\boldsymbol{\sigma}}}$ is a function of the azimuthal angle φ, generally expressed as $\underline{\underline{\boldsymbol{\sigma}}}(\varphi)$. We start by describing all the relevant quantities $\boldsymbol{E}, \boldsymbol{H}$, and $\underline{\underline{\boldsymbol{\sigma}}}$ using their Fourier series in φ. For each specific mode n we use the matrices defined in Eqs. (6a), (6b), and (7) to represent the fields using the corresponding coefficients $\boldsymbol{D}_n$, yielding

$$\begin{pmatrix} E^i_\varphi \\ E^i_z \end{pmatrix} = \sum_{n=-\infty}^{\infty} \underline{\underline{\boldsymbol{M}}}_{E,n}\boldsymbol{D}_n e^{-jn\varphi}, \quad (9a)$$

$$\hat{\boldsymbol{r}} \times \begin{pmatrix} H^o_\varphi - H^i_\varphi \\ H^o_z - H^i_z \end{pmatrix} = \sum_{n=-\infty}^{\infty} \underline{\underline{\boldsymbol{M}}}_{H,n}\boldsymbol{D}_n e^{-jn\varphi}, \quad (9b)$$

and for the conductivity

$$\eta\underline{\underline{\boldsymbol{\sigma}}} = \sum_{m=-\infty}^{\infty} \underline{\underline{\boldsymbol{Y}}}_m e^{-jm\varphi}. \quad (10)$$

When $\underline{\underline{\boldsymbol{\sigma}}} = \underline{\underline{\boldsymbol{\sigma}}}(\varphi)$, coupling exists between different components with different n, through the additional OAM provided by the geometrical structure of $\underline{\underline{\boldsymbol{\sigma}}}$, and we can derive the modal equation by substituting these expansions into Eq. (2),

$$\sum_{n=-\infty}^{\infty} \underline{\underline{\boldsymbol{Y}}}_{\ell-n}\underline{\underline{\boldsymbol{M}}}_{E,n}\boldsymbol{D}_n - \underline{\underline{\boldsymbol{M}}}_{H,\ell}\boldsymbol{D}_\ell = 0 \quad \forall\, \ell, \quad (11)$$

where each value of ℓ represents a row in a 2×2 infinite block matrix. This can be reformulated into a matrix equation, as shown in Appendix B.

For this system to have a nontrivial solution, the determinant of the matrix (B1) must vanish, giving the dispersion equation for the propagating modes. Naturally, since different values of n are coupled through the angle-dependent conductivity of the tube, the modes will be composed of many angular harmonics excited and propagating together. This is in addition to the natural TE/TM coupling in higher-order modes propagating on impedance cylinders, giving rise to hybrid-type modes that can yield interesting patterns of spin and helicity [10].

For the sake of simplicity, we will limit our discussion here to conductivity matrices of the form

$$\underline{\underline{\boldsymbol{\sigma}}}(\varphi) = \underline{\underline{\boldsymbol{\sigma}}}_0 + \underline{\underline{\boldsymbol{\sigma}}}_1 \cos\varphi = \underline{\underline{\boldsymbol{\sigma}}}_0 + \tfrac{1}{2}\left(\underline{\underline{\boldsymbol{\sigma}}}_1 e^{j\varphi} + \underline{\underline{\boldsymbol{\sigma}}}_1 e^{-j\varphi}\right). \quad (12)$$

This will allow us to simplify Eq. (11) and its matrix representation (B1) to a tridiagonal block form. In this case, one could formally express the dispersion relation in a matrix continued fraction form in a process similar to the one described in [24],

$$\begin{aligned} &\underline{\underline{\boldsymbol{Y}}}_1^{-1}[-\underline{\underline{\boldsymbol{Y}}}_0 + \underline{\underline{\boldsymbol{G}}}_n + [-\underline{\underline{\boldsymbol{Y}}}_0 + \underline{\underline{\boldsymbol{G}}}_{n-1} + [\underline{\underline{\boldsymbol{Y}}}_0 + \underline{\underline{\boldsymbol{G}}}_{n-2} + [\cdots]^{-1}]^{-1}]^{-1}] \\ &\quad = \left[\underline{\underline{\boldsymbol{Y}}}_1^{-1}\underline{\underline{\boldsymbol{Y}}}_0 - \underline{\underline{\boldsymbol{Y}}}_1^{-1}\underline{\underline{\boldsymbol{G}}}_{n+1} + \left[\underline{\underline{\boldsymbol{Y}}}_1^{-1}\underline{\underline{\boldsymbol{Y}}}_0 - \underline{\underline{\boldsymbol{Y}}}_1^{-1}\underline{\underline{\boldsymbol{G}}}_{n+2} + [\cdots]^{-1}\right]^{-1}\right]^{-1}, \end{aligned} \quad (13)$$

where $\underline{\underline{\boldsymbol{G}}}_n = \underline{\underline{\boldsymbol{M}}}_{H,n}\underline{\underline{\boldsymbol{M}}}^{-1}_{E,n}$ and we have assumed $\underline{\underline{\boldsymbol{Y}}}_1 = \underline{\underline{\boldsymbol{Y}}}_{-1}$ as in our simplified case.

Since we would like to study nonreciprocal propagation, it is worth noticing that when the guiding structure is reciprocal (satisfying $\underline{\underline{\boldsymbol{\sigma}}} = \underline{\underline{\boldsymbol{\sigma}}}^T$), inverting the propagation direction will result in time-reversed modal fields. For a specific mode, the modal fields will be transformed as $\boldsymbol{E}(-\beta) = \boldsymbol{E}(\beta)^*$ and $\boldsymbol{H}(-\beta) = -\boldsymbol{H}^*(\beta)$. However, this is no longer the case when the conductivity tensor does not satisfy reciprocity. In many cases, merely violating the reciprocity of the guiding structure is not enough for visible effects of nonreciprocity to manifest in the guided modes (such as a nonsymmetric dispersion curve or different field profiles for oppositely propagating waves). This is one of the reasons that [23] did not observe any significant nonreciprocal propagation and excitation effects, despite studying a nonreciprocal structure. However, we will see that more significant nonreciprocal effects are possible in our case due to the explicit geometrical asymmetry arising from the φ dependence of the conductivity matrix.

C. Transversely magnetized gyrotropic tube

The case we focus on is the one in which the conductivity of the cylinder can be expressed as

$$\underline{\underline{\boldsymbol{\sigma}}}(\varphi) = \frac{1}{\eta_0}\begin{pmatrix} jX & X_o\cos\varphi \\ -X_o\cos\varphi & jX \end{pmatrix}. \tag{14}$$

Although this choice seems quite specific, such a system naturally arises if we envision a graphene tube and magnetize it perpendicularly to the cylinder axis, as shown in Fig. 1(a) (in a setup similar to those in [13,25], for instance). When a planar graphene sheet in the YZ plane is subject to a static magnetic field bias $B_0\hat{x}$, its surface conductivity matrix becomes gyrotropic and can be calculated using the Kubo formula [26]. Here, to simplify the analysis, we operate in a regime where we can use a Drude model approximation for the conductivity [27,28] and obtain

$$\sigma_{yy} = \sigma_{zz} = \sigma_0\frac{1+j\omega\tau}{(\omega_c\tau)^2+(1+j\omega\tau)^2}, \tag{15}$$

$$\sigma_{yz} = -\sigma_{zy} = \sigma_0\frac{\omega_c\tau}{(\omega_c\tau)^2+(1+j\omega\tau)^2}, \tag{16}$$

where σ_0 is the DC conductivity of graphene, τ is the scattering time, and $\omega_c = eB_\perp v_f^2/\mu_c$ is the cyclotron frequency ($B_\perp$ is the magnetic bias component perpendicular to the graphene surface, e is the electron charge, v_f is the Fermi velocity, and μ_c is the chemical potential). From these expressions we see that the magnitude of the off-diagonal conductivity term is proportional to the magnetic field component perpendicular to the surface. In our case, when the geometry is cylindrical and the external magnetic field is uniform, $\boldsymbol{B} = B_0\hat{x}$, $B_\perp$ will be a function of φ, $B_\perp = B_0\cos\varphi$, yielding a φ varying matrix, where the in-plane directions are now $\hat{z}$ and $\hat{\varphi}$ [see Eq. (3)]. Due to the bias magnetic field, the diagonal terms will also depend slightly on φ in addition to the denominators in Eqs. (16) and (15). However, for magnetic fields up to $1.5T$ this "extra" dependence is relatively weak (<10% deviation from the value without magnetic field). Therefore, we will neglect this dependence, taking X in Eq. (14) to be independent of φ and approximating the off-diagonal terms using only the φ dependence of the nominator. This variation can be accounted for straightforwardly using the same formulation by simply adjusting the expansion in Eq. (10), but we would like to keep the analysis as simple as possible. To analyze this system using the developed formulation, we represent the conductivity tensor using its φ Fourier transform. The matrix coefficients are

$$\underline{\underline{\boldsymbol{Y}}}_0 = \begin{pmatrix} jX & 0 \\ 0 & jX \end{pmatrix}, \quad \underline{\underline{\boldsymbol{Y}}}_{-1} = \underline{\underline{\boldsymbol{Y}}}_1 = \frac{1}{2}\begin{pmatrix} 0 & -X_o \\ X_o & 0 \end{pmatrix}. \tag{17}$$

Once (17) is substituted into Eq. (11) [or (B1)], we obtain a tridiagonal block system of equations. Although the magnetic bias makes this system nonreciprocal, we know from previous works that nonreciprocity can manifest in several ways, which are often quite subtle.

The conductivity matrix elements for graphene are shown in Fig. 1(b). The parameters we take are the Fermi velocity $v_F = 10^6$ m/s, the chemical potential $\mu_c = 0.35$ V, and a biasing magnetic field of $B_0 = 1.5$ T. Since the response of graphene can be quite lossy in the frequency regions where the gyrotropic effect is significant (yielding meaningful off-diagonal conductivity terms), we want to choose our frequency such that the losses are not too significant as to mask the guided wave propagation. Here, the operation frequency we choose is 4 THz, corresponding to $X \approx -0.6j + 0.135$ and $X_o \approx -0.093 - 0.043j$.

III. DISPERSION

A. Unmagnetized tube

In the unmagnetized case, the dispersion for each value of OAM n can be solved separately [corresponding to the matrix in Eq. (B1) being block diagonal]. Following Eq. (8), the dispersion equation can be written as

$$\det\left[\eta\underline{\underline{\boldsymbol{\sigma}}}\,\underline{\underline{\boldsymbol{M}}}_{E,n} - \underline{\underline{\boldsymbol{M}}}_{H,n}\right] = 0. \tag{18}$$

The dispersion curves for this case are shown using thick dotted blue lines in Fig. 1(c). A degeneracy for positive and negative values of n exists, and both $n = 1$ and $n = -1$ have the same dispersion. In our case, the unmagnetized tube conductivity is scalar, and therefore, for $n = 0$ (and only for this value), Eq. (18) can be completely separated to TE/TM, where only one of them will constitute the propagating mode according to the sign of the imaginary value of σ (the sign of X). Here, we use $\mathrm{Im}[\sigma] < 0$ (an inductive surface), and therefore, the $n = 0$ mode will be a TM mode, with $B_0^i = 0$. For $n \neq 0$, there is always some "mixing" between the TE and TM constituents, although a TM component will still dominate the modes due to the inductive response. The dispersion curve is symmetric due to reciprocity in this case, and therefore, only $\beta > 0$ is presented.

B. Magnetized tube

When applying the magnetic bias, several effects come into play. First, $\underline{\underline{\boldsymbol{\sigma}}}$ is no longer uniform and depends on φ. This creates coupling between different values of OAM, so we can no longer separate the dispersion equations for distinct values of n. Consequently, each modal field distribution, derived from the eigenvector of a certain solution of the dispersion equation, will be composed of contributions from several n's. Usually, significant contributions will come from only one or a few n, but at least theoretically, all of them are a part of the modal field. For this reason, the magnitude of the modal field will no longer be uniform across φ (as expected in the unmagnetized case for a simple $e^{jn\varphi}$ dependence). It is worth mentioning that this is not related to the nonreciprocal response of the magnetized tube but to the cross-sectional inhomogeneity of the conductivity matrix. However, due to the nonreciprocity, this is expected to happen in a nonsymmetric way—propagating modes with $\beta > 0$ and $\beta < 0$ are expected to possess differently distributed fields. This opens the possibility of directional excitation of waves by arbitrary sources, as will be shown later.

The dispersion curve for a magnetized cylinder, with $B_0 = 1.5$ T, is shown by solid magenta lines in Fig. 1(c), where we have neglected the associated losses to obtain a clear modal dispersion. Due to the coupling between different OAM values and the nonreciprocity, the degeneracy is now broken, and the $n = \pm 1$ branch splits into two separate branches. The $n = 0$ branch, which was not degenerate in

the first place, experiences some frequency shift. For this calculation, the infinite matrix dispersion equation was truncated at $n = \pm 7$, which is enough for the specific modes in our examples. Higher-order modes might require a different truncation. The dispersion remains symmetric in this case due to the fact that time-reversal yields the same structure, rotated 180°; therefore, we retain only the $\beta > 0$ portion.

The calculation of this dispersion assumes that the conductivity values did not change as a function of k_0R. Therefore, the vertical axis can be seen as a variation of the cylinder radius, for instance. A variation in the frequency would require that we also vary the conductivity matrix (both the diagonal and off-diagonal terms depend on frequency). An example of the surface wave dispersion when considering this dependence $\underline{\underline{\sigma}}(\omega)$ is shown in green in Fig. 1(c). We see that qualitatively, the curves are similar, yet there is a difference in the obtained wave numbers due to the varying conductivity values for different frequencies. The radius of the tube is taken to be $R = 6$ μm here. The dashed black line indicates the operation frequency for which we later calculate the fields in different scenarios.

To illustrate the modal fields, we calculate the modal coefficients. The operation point was chosen to be $k_0R \approx 0.5$, corresponding to a cylinder with radius $R = 6\,\mu$m in $f = 4$ THz. Figure 2 shows the longitudinal fields $|E_z|$ and $|H_z|$ for the three modes that solve the presented dispersion. Figures 2(a) and 2(b) show the modes that split from the $n = \pm 1$ branch, presenting a mixed TE/TM nature. The mode close to the $n = 0$ branch, shown in Fig. 2(c), is TM dominated (notice the relatively weaker H_z content) since around this regime, the TE/TM coupling is weaker, a remnant of the pure TM $n = 0$ mode in the unmagnetized case. The thin lines in Fig. 2(c) show the modal fields for $\beta < 0$, and we see a significant difference in the field distribution compared to $\beta > 0$, a clear consequence of the nonreciprocity (in the reciprocal case, we would expect a simple conjugation operation, which would preserve the profile of $|E_z|$ and $|H_z|$). The electric field oscillates "slowly" since the $n = 0$ coefficient still dominates it, but the magnetic field oscillates more rapidly since the magnetic fields are dominated by the $n = \pm 1$ coefficients, coupled through the nonuniform conductivity. This is confirmed in Fig. 2(d), where we see the coefficients composing the field corresponding to the mode shown in Fig. 2(c).

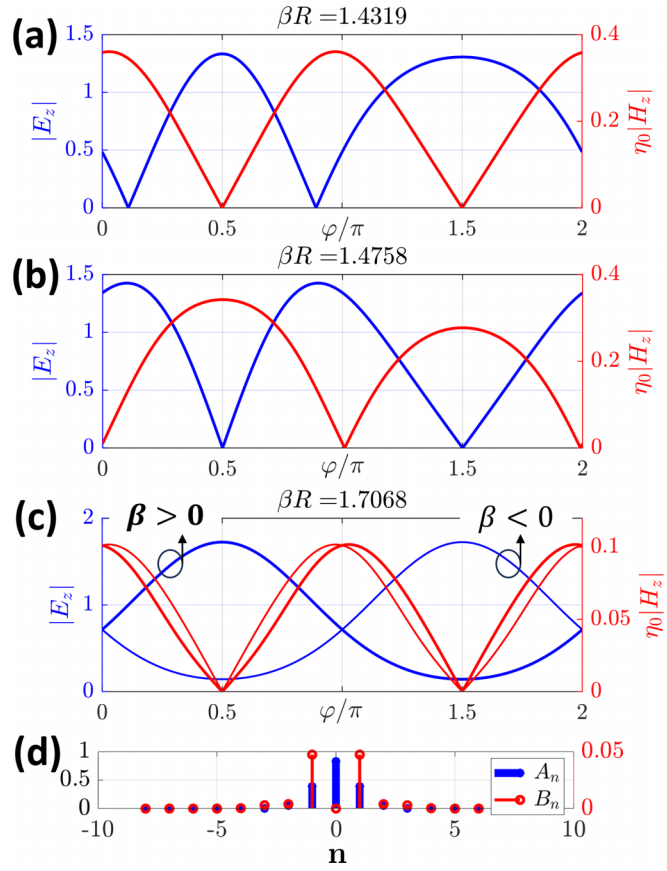

FIG. 2. Mode field profiles for a magnetized graphene cylinder. (a) and (b) show the modes that split from the degenerate $n = \pm 1$ mode in the unmagnetized case. (c) The perturbed $n = 0$ mode. Thin lines show the field profiles for $\beta < 0$, displaying significant asymmetry. (d) The modal coefficients A_n and B_n for the mode shown in (c).

IV. EXCITATION OF WAVES

We performed full-wave simulations of different excitation schemes to illustrate the various aspects of this system using COMSOL MULTIPHYSICS [29]. Throughout this section, we use the operation point previously introduced, $f = 4$ THz, $R = 6$ μm, and $B_0 = 1.5$ T, unless explicitly stated otherwise. The magnetically biased graphene is represented in the simulation using the surface conductivity boundary condition, with the explicit coordinate dependence given in Eq. (14). The length of the simulated tube is $L = 150$ μm [see the horizontal axis in Fig. 3(c)], mostly limited by the computational power available to us.

A. Excitation centered around a specific OAM

We start by inspecting the fields excited by a source centered on a specific value of n. To this end, we used a ring surrounding the magnetized tube, with a radius of $1.1R$, as shown in Fig. 3(a). On this ring, we applied a surface current $\boldsymbol{J}_s = \hat{z}e^{-jn\varphi}$ and examined the excited fields. Figure 3(b) shows the profile of E_z and H_z, similar to Fig. 2. The dashed line shows the distribution obtained from the full-wave simulation, and the solid line shows the analytical result for comparison. We see a good match between the field profiles since the analytically obtained electric field mainly comprises the $n = 0$ component. It is worth mentioning that while the field distributions along φ are very similar, they are not identical (in terms of the ratio between the field magnitudes, for instance). This is because we cannot excite a single mode this way, and the propagating fields contain at least some contribution from other modes. In Fig. 3(c), we see how propagation to the $+\hat{z}$ direction has fields that are most dominant on the upper side (corresponding to $\varphi = \pi/2$), whereas in propagation to $-\hat{z}$ the lower side is more dominant. This is, again, a direct consequence of the system nonreciprocity and would not occur if the system response were reciprocal (even if it were strongly dependent on φ or even anisotropic). From

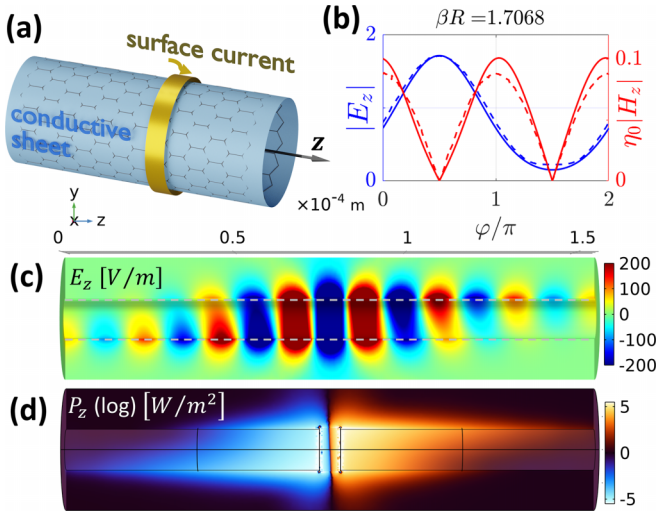

FIG. 3. (a) The surface current source is placed on the yellow ring around the cylinder. (b) Dashed lines show the simulated $\hat{z}$ component of the propagating fields excited by the source with $n = 0$ as a function of φ, measured on a circle in the XY plane with radius $1.1R$, placed $L/3$ from the source along the $+\hat{z}$ axis. Solid lines show the analytical field distribution of the $n = 0$ mode. (c) Distribution of the excited electric field longitudinal component E_z. The guiding cylinder is between the dashed lines. (d) The $\hat{z}$ component of the Poynting vector P_z on a logarithmic scale. The sign was added to indicate the direction of power flow.

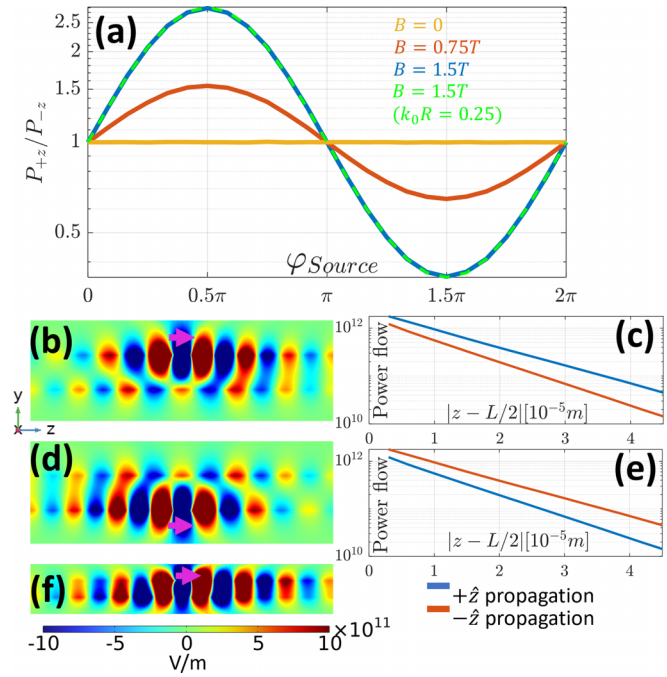

FIG. 4. (a) Ratio between the total power passing through the tube cross section in the $+z$ and $-z$ directions as a function of the location of the dipole source around the cylinder $[x_s, y_s]$. (b) E_z for $\phi_s = \pi/2$; the source dipole is shown in magenta. The asymmetry is visible. (c) Total power flow to $\pm\hat{z}$ vs distance from the source ($\phi_s = \pi/2$). (d) Same as (b), but for $\phi_s = 3\pi/2$. (e) Same as (c), but for $\phi_s = 3\pi/2$. (f) E_z for a smaller cylinder, with $k_0R \approx 0.25$.

Fig. 3(c) we are also able to approximate the wavelength of the propagating wave, and it corresponds to $\beta R \approx 1.6$, which is close to the value we extract from the analytical formulation, $\beta R \approx 1.7$. The inaccuracy is caused by the coupling of various modes in the numerical simulation. Figure 3(d) confirms the power flow also obtains the same asymmetric pattern—the flow towards the right (left) is on the upper (lower) side of the tube.

B. Excitation by a point source

Next, we would like to understand how the modal properties manifest when exciting the system with a point source. When using a point source, in principle, a superposition of all possible wave species is excited, each with a different amplitude. With such excitation, we can feel the system properties as a whole, essentially "probing" the Green's function. We would like to examine the asymmetric excitation of waves as a demonstration for nonreciprocity. Reciprocal structures, such as bianisotropic metamaterials, can also be excited in a directional way. In reciprocal systems where this is possible, it would always require excitation by a source that is not time reversal symmetric (for instance, circularly polarized dipoles [30–32] or combinations of electric and magnetic dipoles [33]). Due to the nonreciprocity in our case, we get pronounced asymmetry in the propagation of power even with simple sources (which are time reversal symmetric) since the field distributions of the modes that propagate in opposite directions are significantly different. We simulated the fields excited by a dipole source $\boldsymbol{p} = p\hat{z}$ in different locations $[x_s, y_s]$ around the center of the cylindrical waveguide, $x_s = 1.1R\cos\varphi_s$ and $y_s = 1.1R\sin\varphi_s$, with z_s being in the central plane, $z_s = L/2$. We then calculated the total power flowing through two cross sections at $z = L/4$ and $z = 3L/4$. Figure 4(a) shows the ratio between the power that propagates in the $+z$ and $-z$ directions—the isolation ratio—as a function of the source location angle φ_s for different values of the magnetic bias. Significant nonreciprocity is present, with $\phi_s = \pi/2, 3\pi/2$ having the strongest asymmetry in power propagation. In Fig. 4(b) [Fig. 4(d)] we see the propagating fields for $\phi_s = \pi/2$ ($\phi_s = 3\pi/2$). The asymmetry is visible, and it is worth mentioning that this propagating power is not a result of a single propagating mode but all of the possible ones (three in this case). Evidence of this can be seen from the "inconsistent" wave fronts in both panels since the excited modes also have different attenuation and propagation constants. In Figs. 4(c) and 4(e) we see the total power propagating towards $\pm\hat{z}$ as a function of the cross-section distance from the source. The initially launched power is visibly asymmetric, and we also notice the different decay rates due to the different mixture of modes, which also favors the "allowed" propagation direction. Examining the dispersion, we see that for $k_0R < 0.3$ we can obtain a "single-mode" operation regime. Figure 4(f) shows the propagating fields for this case when the source is placed at $\phi_s = \pi/2$, and we can see the much more uniform wave fronts. Although the asymmetry in the field picture might not seem as pronounced, calculating the $+z$ to $-z$ propagating power reveals a similar picture, as shown by the dashed green line in Fig. 4(a). This demonstrates that isolation is a

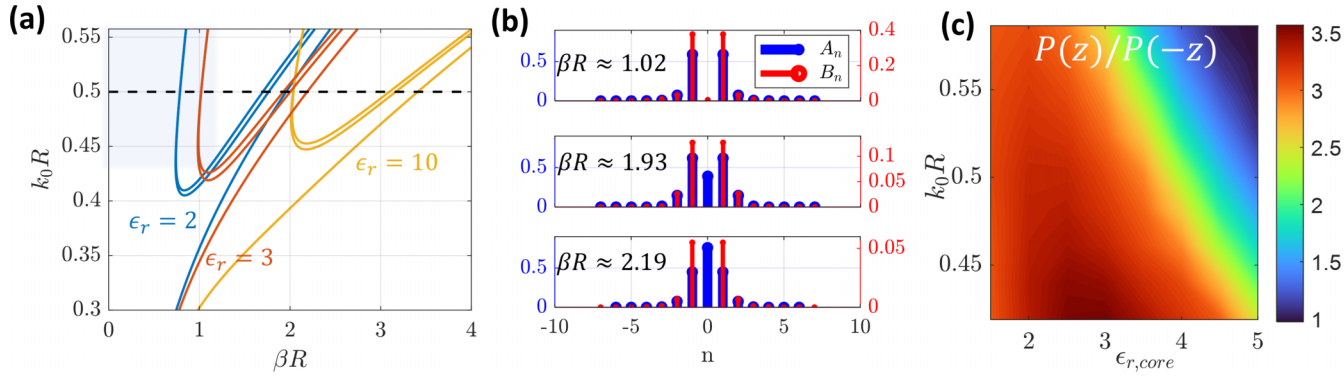

FIG. 5. (a) Surface wave dispersion when the graphene sheet is wrapped around a dielectric core for $\epsilon_{r,\text{core}} = [2, 3, 10]$. (b) Modal TE/TM composition for three modes (out of five seen on the dispersion curve) when $\epsilon_r = 3$. (c) The maximal isolation ratio (essentially, the isolation ratio for $\phi_s = \pi/2$) vs ϵ_r of the core and the radius of the tube. For each R (a horizontal cross section) there is an optimal ϵ_r which delivers the best isolation.

fundamental phenomenon here and is not dependent the "mixed" excitation of modes.

V. A MAGNETIZED TUBE WRAPPED AROUND A DIELECTRIC CORE

When the conductive sheet is wrapped around a dielectric core, the value of α in Eqs. (1a) and (1b) differs between the inner and outer parts, which we will term $\alpha_{i,o}$. If the core has a dielectric constant of ϵ_r, we will have $\beta^2 = \alpha_i^2 + \epsilon_r k_0^2$ and $\beta^2 = \alpha_o^2 + k_0^2$. Substituting these into the same equations and performing manipulations similar to the ones shown in Appendix A yield the same infinite matrix relation shown in Appendix B, with the reformulated building blocks

$$\underline{\underline{\boldsymbol{M}}}_{E,n} = \begin{bmatrix} \frac{n\bar{\beta}}{\bar{\alpha}_i^2} I_n & -\frac{j\bar{k}_0\sqrt{\epsilon_r}}{\bar{\alpha}_i} I_n' \\ I_n & 0 \end{bmatrix}, \quad \underline{\underline{\boldsymbol{M}}}_{H,n} = \underline{\underline{\boldsymbol{M}}}^o_{H,n} - \underline{\underline{\boldsymbol{M}}}^i_{H,n}, \tag{19}$$

where

$$\underline{\underline{\boldsymbol{M}}}^i_{H,n} = \frac{1}{\eta_0} \begin{bmatrix} 0 & -I_n\sqrt{\epsilon_r} \\ \frac{j\bar{k}_0\sqrt{\epsilon_r}}{\bar{\alpha}_i} I_n' & \frac{n\bar{\beta}\sqrt{\epsilon_r}}{\bar{\alpha}^2} I_n \end{bmatrix} \tag{20}$$

and

$$\underline{\underline{\boldsymbol{M}}}^o_{H,n} = \frac{1}{\eta_0} \begin{bmatrix} \frac{K_n}{K_n'} \frac{n\bar{\beta}\bar{\alpha}_o}{j\bar{k}_0} I_n \Delta & -\sqrt{\epsilon_r}\frac{\alpha_o}{\alpha_i}\frac{I_n' K_n}{K_n'} \\ \frac{j\bar{k}_0}{\bar{\alpha}_o}\frac{I_n K_n'}{K_n} - \frac{(n\bar{\beta})^2}{j\bar{k}_0\eta_0\bar{\alpha}_o}\frac{K_n I_n}{K_n'}\Delta & \frac{n\bar{\beta}\sqrt{\epsilon_r}}{\bar{\alpha}_o\bar{\alpha}_i}\frac{I_n' K_n}{K_n'} \end{bmatrix}. \tag{21}$$

Here, $\Delta = (\frac{1}{\bar{\alpha}_i^2} - \frac{1}{\bar{\alpha}_o^2})$, which is indicative of the material contrast between the core and the surroundings, $I_n = I_n(\alpha_i R)$, $K_n = K_n(\alpha_o R)$ and $I_n' = dI_n(x)/dx|_{x=\alpha_i R}$, $K_n' = dK_n(x)/dx|_{x=\alpha_o R}$. The parameters η and k are the intrinsic impedance and wave number of the dielectric medium, and k_0 and η_0 are those of vacuum. One can see that when substituting $\epsilon_r = 1$, we get $\alpha_i = \alpha_o$ and $\eta = \eta_0$, and we revert back to Eqs. (7). The solutions are obtained in the same way as in the previous case by substituting the graphene conductivity and $\underline{\underline{\boldsymbol{M}}}_{E,n}$ and $\underline{\underline{\boldsymbol{M}}}_{H,n}$ into Eq. (B1).

Figure 5(a) shows the dispersion relation for a dielectric core with $\epsilon_r = [2, 3, 10]$. The first difference we notice with respect to the all-vacuum case is that new modes emerge that did not exist previously. These modes are much less confined to the tube located in the shaded region in the top left corner of the dispersion plot. We see almost no "split" in their wave number since the split is induced by the properties of the angularly varying conductivity, and being less confined, their interaction with the graphene shell is much weaker. As expected, increasing the dielectric constant of the core gives larger values of α and shorter wavelengths of the guided waves. In Fig. 5(b), we see the contribution of the different angular components. On the top, we see the new low-confinement mode. Due to its weak interaction with the graphene layer, there is much less coupling between different values of n (we see mainly the ± 1 components), and the mode is much more balanced in the TE/TM sense. In the more confined modes [bottom two panels in Fig. 5(b)], the interaction with the graphene is stronger, which leads to a more pronounced TM nature and stronger coupling between different n.

The core dielectric constant also affects the isolation ratio. We examine it in a manner similar to the way we examined Fig. 4(a), additionally considering the ϵ_r degree of freedom. The dynamics of the isolation ratio as a function of the source angle φ_s (or, equivalently, the magnetic field direction in the XY plane) is qualitatively the same as Fig. 4(a), and therefore, we focus on the maximal isolation ratio, obtained for $\varphi_s = \pi/2$. Figure 5(c) shows the maximal isolation in the $[\epsilon_r, k_0R]$ plane. Interestingly, we see that for a certain value of k_0R there is an optimal choice for ϵ_r which yields the best isolation. This is caused by the fact that increasing ϵ_r causes several competing effects. It increases the field confinement (by increasing β), which enhances the interaction of waves with the nonreciprocal graphene, boosting the nonreciprocal effect. On the other hand, the same increased interaction makes the propagating waves more prone to losses, increasing decay of the fields and altering the spectral mixture of the propagating waves. It is also important to note that the details of this "map" depend on other parameters such as the choice of planes where we integrate the power [as can be seen in Figs. 4(c) and 4(e)] and the distance of the source from the tube.

VI. CONCLUSIONS

In this work, we analyzed the wave propagation and the nonreciprocal characteristics of surface waves guided by a cylindrically rolled graphene tube. The tube is biased by a uniform magnetic field, perpendicular to the cylinder axis. The used magnetic biasing scheme is a realistic one, and it results in a system with a nonuniform cross-section conductivity. The resulting propagating modes form a mixture of TE/TM components and several dominant values of OAM. The geometrical asymmetry yields pronounced nonreciprocal effects—a different cross-sectional field distribution for oppositely propagating modes. These were leveraged for a directional excitation of waves using a simple dipole source as a function of the source placement around the tube. Generalizing the analysis for a graphene sheet wrapped on a dielectric core, we saw new modes emerge, poorly confined and weakly interacting with the graphene sheet, in addition to the highly confined surface waves. When exciting the waves with a point source, the dielectric core can yield more pronounced isolation, with demonstrated ratios of around ≈ 3. This can be further improved by adding additional elements, such as an inhomogeneous core or structuring of the graphene layer, which is left for future work. The continuous dependence of the isolation ratio on the direction of the magnetic bias (if we consider the source at a constant position and "rotate" the magnetic bias in the XY plane) lets us tailor the power propagation properties using the magnetic bias direction as an easy control knob without needing to solve for a different bias intensity or redesign the geometry and materials. This component could have several applications, such as acting as a building block for miniature isolators and circulators in the terahertz range, controlling signal flow, enhancing light-matter interaction in graphene-wrapped microfiber systems [18], and acting as a nonreciprocal antenna [23].

ACKNOWLEDGMENT

Y.M. acknowledges support from the Israeli Science Foundation, Grant No. 1089/22.

APPENDIX A: MODAL FIELD DERIVATION

Given the $\hat{z}$ components of the electric and magnetic fields in the TM and TE components, respectively, we can use the following equations to derive the rest of the field components in cylindrical coordinates [1]:

$$E_r = \frac{j}{\alpha^2}\left(\beta\frac{\partial E_z}{\partial r} + \frac{\omega\mu}{r}\frac{\partial H_z}{\partial \varphi}\right), \tag{A1}$$

$$E_\varphi = \frac{j}{\alpha^2}\left(\frac{\beta}{r}\frac{\partial E_z}{\partial \varphi} - \omega\mu\frac{\partial H_z}{\partial r}\right), \tag{A2}$$

$$H_r = -\frac{j}{\alpha^2}\left(\frac{\omega\epsilon}{r}\frac{\partial E_z}{\partial \varphi} - \beta\frac{\partial H_z}{\partial r}\right), \tag{A3}$$

$$H_\varphi = \frac{j}{\alpha^2}\left(\omega\epsilon\frac{\partial E_z}{\partial r} + \frac{\beta}{r}\frac{\partial H_z}{\partial \varphi}\right). \tag{A4}$$

Substituting Eqs. (1a) and (1b) into these relations and applying the continuity boundary condition in Eq. (4) yield

$$I_n A_n^i = K_n A_n^o. \tag{A5}$$

The continuity of E_φ gives

$$\frac{n\beta}{\alpha^2 R}\left[I_n A_n^i - K_n A_n^o\right] - \frac{jk_0}{\alpha}\left[I_n' B_n^i - K_n' B_n^o\right] = 0, \tag{A6}$$

from which we get

$$I_n' B_n^i = K_n' B_n^o. \tag{A7}$$

In Eq. (5), we defined a truncated coefficient column vector $\boldsymbol{D}_n$. Using these relations, the representation of the guided wave fields can be written as

$$E_z^i(r=R) = E_z^o(r=R) = [I_n, 0]\boldsymbol{D}_n e^{-jn\varphi}e^{-j\beta z}, \tag{A8a}$$

$$E_\varphi^i(r=R) = E_\varphi^o(r=R) = \left[\frac{n\beta}{\alpha^2 R}, -\frac{jk_0}{\alpha}I_n'\right]\boldsymbol{D}_n e^{-jn\varphi}e^{-j\beta z}, \tag{A8b}$$

$$H_z^i(r=R) = \left[0, \frac{1}{\eta_0}I_n\right]\boldsymbol{D}_n e^{-jn\varphi}e^{-j\beta z}, \tag{A8c}$$

$$H_z^o(r=R) = \left[0, \frac{1}{\eta_0}\frac{I_n'}{K_n'}K_n\right]\boldsymbol{D}_n e^{-jn\varphi}e^{-j\beta z}, \tag{A8d}$$

$$H_\varphi^i(r=R) = \left[\frac{jk_0}{\alpha\eta_0}I_n', \frac{\beta n}{\alpha^2 R\eta_0}I_n\right]\boldsymbol{D}_n e^{-jn\varphi}e^{-j\beta z}, \tag{A8e}$$

$$H_\varphi^o(r=R) = \left[\frac{jk_0}{\alpha\eta_0}\frac{I_n}{K_n}K_n', \frac{\beta n}{\alpha^2 R\eta_0}\frac{I_n'}{K_n'}K_n\right]\boldsymbol{D}_n e^{-jn\varphi}e^{-j\beta z}. \tag{A8f}$$

These relations can be transformed into a matrix representation which will be instrumental to the convenient analysis of the guided modes, and using the Wronskian identity

$$I_n'(x)K_n(x) - K_n'(x)I_n(x) = \frac{1}{x}, \tag{A9}$$

one can arrive at the definitions given in Eq. (7).

APPENDIX B: INFINITE MATRIX EIGENMODE EQUATION

Equation (11) can be written in an infinite matrix form:

$$\begin{pmatrix} \ddots & \vdots & \vdots & \vdots & \ddots \\ \cdots & \underline{\underline{\boldsymbol{Y}}}_0\underline{\underline{\boldsymbol{M}}}_{E,-1} - \underline{\underline{\boldsymbol{M}}}_{H,-1} & \underline{\underline{\boldsymbol{Y}}}_{-1}\underline{\underline{\boldsymbol{M}}}_{E,0} & \underline{\underline{\boldsymbol{Y}}}_{-2}\underline{\underline{\boldsymbol{M}}}_{E,1} & \cdots \\ \cdots & \underline{\underline{\boldsymbol{Y}}}_1\underline{\underline{\boldsymbol{M}}}_{E,-1} & \underline{\underline{\boldsymbol{Y}}}_0\underline{\underline{\boldsymbol{M}}}_{E,0} - \underline{\underline{\boldsymbol{M}}}_{H,0} & \underline{\underline{\boldsymbol{Y}}}_{-1}\underline{\underline{\boldsymbol{M}}}_{E,1} & \cdots \\ \cdots & \underline{\underline{\boldsymbol{Y}}}_2\underline{\underline{\boldsymbol{M}}}_{E,-1} & \underline{\underline{\boldsymbol{Y}}}_1\underline{\underline{\boldsymbol{M}}}_{E,0} & \underline{\underline{\boldsymbol{Y}}}_0\underline{\underline{\boldsymbol{M}}}_{E,1} - \underline{\underline{\boldsymbol{M}}}_{H,1} & \cdots \\ \ddots & \vdots & \vdots & \vdots & \ddots \end{pmatrix}\begin{pmatrix} \vdots \\ \boldsymbol{D}_{-2} \\ \boldsymbol{D}_{-1} \\ \boldsymbol{D}_0 \\ \boldsymbol{D}_1 \\ \boldsymbol{D}_2 \\ \vdots \end{pmatrix} = 0. \tag{B1}$$

When conductivity of the form given in Eq. (12) is used, this matrix reduces to a tridiagonal block matrix.

[1] R. Collin, *Foundations for Microwave Engineering* (McGraw-Hill, New York, 1992), p. 881

[2] J. D. Kraus and R. J. Marhefka, *Antennas for All Applications*, 3rd ed., McGraw-Hill Series in Electrical Engineering (McGraw-Hill, New York, 2002).

[3] H. D. Levine and C. H. Papas, Theory of the circular diffraction antenna, J. Appl. Phys. **22**, 29 (1951).

[4] Y. R. Padooru, A. B. Yakovlev, P.-Y. Chen, and A. Alú, Analytical modeling of conformal mantle cloaks for cylindrical objects using sub-wavelength printed and slotted arrays, J. Appl. Phys. **112**, 034907 (2012).

[5] C.-W. Lin and A. Grbic, Analysis and synthesis of cascaded cylindrical metasurfaces using a wave matrix approach, IEEE Trans. Antennas Propag. **69**, 6546 (2021).

[6] F. Alpeggiani, K. Y. Bliokh, F. Nori, and L. Kuipers, Electromagnetic helicity in complex media, Phys. Rev. Lett. **120**, 243605 (2018).

[7] J. R. Pierce and P. K. Tien, Coupling of modes in helixes, Proc. IRE **42**, 1389 (1954).

[8] N. Raveu, B. Byrne, L. Claudepierre, and N. Capet, Modal theory for waveguides with anisotropic surface impedance boundaries, IEEE Trans. Microwave Theory Tech. **64**, 1153 (2016).

[9] J. G. Pollock, A. K. Iyer, D. Pratap, and S. A. Ramakrishna, A class of circular waveguiding structures containing cylindrically anisotropic metamaterials: Applications from radio frequency/microwave to optical frequencies, J. Appl. Phys. **119**, 083103 (2016).

[10] Y. Mazor and A. Alù, Angular-momentum selectivity and asymmetry in highly confined wave propagation along sheath-helical metasurface tubes, Phys. Rev. B **99**, 155425 (2019).

[11] C. J. M. Barker, N. D. Zanche, and A. K. Iyer, Dispersion and polarization control in below-cutoff circular waveguides using anisotropic metasurface liners, IEEE Trans. Microwave Theory Tech. **71**, 3392 (2023).

[12] G. Y. Slepyan, S. A. Maksimenko, A. Lakhtakia, O. Yevtushenko, and A. V. Gusakov, Electrodynamics of carbon nanotubes: Dynamic conductivity, impedance boundary conditions, and surface wave propagation, Phys. Rev. B **60**, 17136 (1999).

[13] J.-L. Kou, J. hui Chen, Y. Chen, F. Xu, and Y. Qing Lu, Platform for enhanced light-graphene interaction length and miniaturizing fiber stereo devices, Optica **1**, 307 (2014).

[14] K. Chen *et al.*, Graphene photonic crystal fibre with strong and tunable light–matter interaction, Nat. Photon. **13**, 754 (2019).

[15] Y. Wu, B. C. Yao, Q. Y. Feng, X. L. Cao, X. Y. Zhou, Y. J. Rao, Y. Gong, W. L. Zhang, Z. G. Wang, Y. F. Chen, and K. S. Chiang, Generation of cascaded four-wave-mixing with graphene-coated microfiber, Photonics Res. **3**, A64 (2015).

[16] J.-H. Chen, B.-C. Zheng, G.-H. Shao, S.-J. Ge, F. Xu, and Y.-Q. Lu, An all-optical modulator based on a stereo graphene–microfiber structure, Light: Sci. Appl. **4**, e360 (2015).

[17] I. D. Barcelos, L. G. Moura, R. G. Lacerda, and A. Malachias, Observation of strain-free rolled-up CVD graphene single layers: Toward unstrained heterostructures, Nano Lett. **14**, 3919 (2014).

[18] J.-H. Chen, Y.-F. Xiong, F. Xu, and Y.-Q. Lu, Silica optical fiber integrated with two-dimensional materials: Towards opto-electro-mechanical technology, Light: Sci. Appl. **10**, 78 (2021).

[19] C. Caloz, A. Alù, S. Tretyakov, D. Sounas, K. Achouri, and Z.-L. Deck-Léger, Electromagnetic nonreciprocity, Phys. Rev. Appl. **10**, 047001 (2018).

[20] A. Kord, D. L. Sounas, and A. Alú, Microwave nonreciprocity, Proc. IEEE **108**, 1728 (2020).

[21] Z. Yu, G. Veronis, Z. Wang, and S. Fan, One-way electromagnetic waveguide formed at the interface between a plasmonic metal under a static magnetic field and a photonic crystal, Phys. Rev. Lett. **100**, 023902 (2008).

[22] Y. Mazor, Y. Hadad, and B. Z. Steinberg, Planar one-way guiding in periodic particle arrays with asymmetric unit cell and general group-symmetry considerations, Phys. Rev. B **92**, 125129 (2015).

[23] D. Correas-Serrano, J. S. Gomez-Diaz, A. Alù, and A. Á. Melcón, Electrically and magnetically biased graphene-based cylindrical waveguides: Analysis and applications as reconfigurable antennas, IEEE Trans. Terahertz Sci. Technol. **5**, 951 (2015).

[24] A. Oliner and A. Hessel, Guided waves on sinusoidally-modulated reactance surfaces, IRE Trans. Antennas Propag. **7**, 201 (1959).

[25] C. Li, J.-H. Chen, S.-C. Yan, F. Xu, and Y.-Q. Lu, A fiber laser using graphene-integrated 3-D microfiber coil, IEEE Photon. J. **8**, 1 (2016).

[26] R. Kubo, Statistical-mechanical theory of irreversible processes. I. General theory and simple applications to magnetic and conduction problems, J. Phys. Soc. Jpn. **12**, 570 (1957).

[27] V. P. Gusynin, S. G. Sharapov, and J. P. Carbotte, On the universal ac optical background in graphene, New J. Phys. **11**, 095013 (2009).

[28] D. L. Sounas and C. Caloz, Gyrotropy and nonreciprocity of graphene for microwave applications, IEEE Trans. Microwave Theory Tech. **60**, 901 (2012).

[29] COMSOL AB, COMSOL MULTIPHYSICSÂ® version 6.2, COMSOL AB, Stockholm (2024).

[30] M. Onoda, S. Murakami, and N. Nagaosa, Hall effect of light, Phys. Rev. Lett. **93**, 083901 (2004).

[31] F. J. Rodríguez-Fortuño, G. Marino, P. Ginzburg, D. O'Connor, A. Martínez, G. A. Wurtz, and A. V. Zayats, Near-field interference for the unidirectional excitation of electromagnetic guided modes, Science **340**, 328 (2013).

[32] Y. Mazor and A. Alù, Routing optical spin and pseudospin with metasurfaces, Phys. Rev. Appl. **14**, 014029 (2020).

[33] M. F. Picardi, A. V. Zayats, and F. J. Rodríguez-Fortuño, Janus and huygens dipoles: Near-field directionality beyond spin-momentum locking, Phys. Rev. Lett. **120**, 117402 (2018).